American Mineralogist, Volume 106, pages 762–773, 2021

Constraints on deep, CO_2-rich degassing at arc volcanoes from solubility experiments on hydrous basaltic andesite of Pavlof Volcano, Alaska Peninsula, at 300 to 1200 MPa

Margaret T. Mangan[1], Thomas W. Sisson[1,*], W. Ben Hankins[1], Nobumichi Shimizu[2], and Torsten Vennemann[3]

[1]U.S. Geological Survey, 345 Middlefield Road, Mail Stop 310, Menlo Park, California 94025, U.S.A.
[2]Woods Hole Oceanographic Institution, Mail Stop 23, 266 Woods Hole Road, Woods Hole, Massachusetts 02543-1050, U.S.A.
[3]University of Lausanne, Institute of Earth Surface Dynamics, CH-1015 Lausanne, Switzerland

Abstract

The solubility of CO_2 in hydrous basaltic andesite was examined in f_{O_2}-controlled experiments at a temperature of 1125 °C and pressures between 310–1200 MPa. Concentrations of dissolved H_2O and CO_2 in experimental glasses were determined by ion microprobe calibrated on a subset of run glasses analyzed by high-temperature vacuum manometry. Assuming that the solubility of H_2O in mafic melt is relatively well known, estimates of $X_{H_2O}^{fluid}$ and $P_{H_2O}^{fluid}$ in the saturating fluid were modeled, and by difference, values for $X_{CO_2}^{fluid}$ and $P_{CO_2}^{fluid}$ were obtained (X_{CO_2} ~0.5–0.9); f_{CO_2} could be then calculated from the fluid composition, temperature, and pressure.

Dissolved H_2O over a range of 2.3–5.5 wt% had no unequivocal influence on the dissolution of CO_2 at the pressures and fluid compositions examined. For these H_2O concentrations, dissolved CO_2 increases with f_{CO_2} following an empirical power-law relation: dissolved CO_2 (ppmw) = $14.9^{+4.5}_{-3.3}[f_{CO_2}$ (MPa)]$^{0.7\pm0.03}$. The highest-pressure results plot farthest from this equation but are within its 1 standard-error uncertainty envelope.

We compare our experimental data with three recent CO_2-H_2O solubility models: Papale et al. (2006); Iacono-Marziano et al. (2012); and Ghiorso and Gualda (2015). The Papale et al. (2006) and Iacono-Marizano et al. (2012) models give similar results, both over-predicting the solubility of CO_2 in a melt of the Pavlof basaltic andesite composition across the f_{CO_2} range, whereas the Ghiorso and Gualda (2015) model under-predicts CO_2 solubility. All three solubility models would indicate a strong enhancement of CO_2 solubility with increasing dissolved H_2O not apparent in our results. We also examine our results in the context of previous high-pressure CO_2 solubility experiments on basaltic melts. Dissolved CO_2 correlates positively with mole fraction (Na+K+Ca)/Al across a compositional spectrum of trachybasalt-alkali basalt-tholeiite-icelandite-basaltic andesite. Shortcomings of current solubility models for a widespread arc magma type indicate that our understanding of degassing in the deep crust and uppermost mantle remains semi-quantitative. Experimental studies systematically varying concentrations of melt components (Mg, Ca, Na, K, Al, Si) may be necessary to identify solubility reactions, quantify their equilibrium constants, and thereby build an accurate and generally applicable solubility model.

Keywords: Experimental petrology, magmatic CO_2, volcanic degassing, volatile solubility

Introduction

Many studies address the systematics of magmatic degassing in shallow crustal reservoirs and volcanic conduits, yet few are focused on degassing in the deep roots of volcanic systems. Understanding the behavior of C-O-H supercritical fluids in sub-arc magma at elevated pressures is important to a diverse suite of topics. Such knowledge is required to accurately assess volcanic volatile budgets and magma supply rates; model the linkage between basaltic underplating and remobilization of crystal mushes; interpret deep, long-period seismicity and tremor; and to characterize the thermodynamics of lower crustal melting.

Continued progress on these, and a host of other important research fronts, necessitate a more comprehensive and quantitative assessment of CO_2 solubility in hydrous mafic magmas at deep- to mid-crustal conditions. Due to the complexity of high-temperature and high-pressure experiments using mafic melts, relevant data are limited to a handful of studies—Jakobsson (1997); Liu et al. (2006); Botcharnikov et al. (2005); Behrens et al. (2009); Shishkina et al. (2010); Vetere et al. (2011); Iacono-Marziano et al. (2012); Iacovino et al. (2013); Allison et al. (2019)—and the thermodynamic and empirical models used to predict C-O-H solubilities in magma at pressures above ~500 MPa (e.g., Papale et al. 2006; Iacono-Marziano 2012; Duan 2014; Ghiorso and Gualda 2015) have scant data to constrain them.

With the intent of building a stronger framework for understanding deep, CO_2-rich degassing of sub-arc magma, we conducted f_{O_2}-buffered solubility experiments at 1125 °C between

* E-mail: tsisson@usgs.gov. Orcid 0000-0003-3380-6425

0003-004X/21/0005–762$05.00/DOI: https://doi.org/10.2138/am-2021-7531

310 to 1200 MPa total pressure using a hydrated basaltic andesite lava from Pavlof volcano, one of the most active centers in the Alaskan Aleutian Arc. We also conducted a small subset of decompression experiments to assess the ease of degassing and CO_2 re-equilibration during magma ascent.

Our oxygen-buffered, fluid-saturated experiments involved equilibration and degassing of fully molten natural basaltic andesite with C-O-H fluids in a piston-cylinder apparatus in the U.S. Geological Survey (USGS) Magma Dynamics Laboratory in Menlo Park, California. Volatile concentrations were measured in the quenched melts via ion microprobe calibrated with a subset of glasses with dissolved H_2O and CO_2 concentrations determined by high-temperature vacuum manometry. A few runs were also examined by Fourier-transform infrared spectroscopy (FTIR), but this method proved imprecise at the high dissolved CO_2 concentrations. Compositions of the excess fluid in equilibrium with the melt were estimated by application of relatively well-known H_2O solubility relations, as described subsequently.

Methods

Experimental techniques

The experiments use a natural basaltic andesite lava erupted from Pavlof volcano, one of six overlapping arc-front volcanoes within the Quaternary Emmons Lake Volcanic Center on the lower Alaska Peninsula (Mangan et al. 2009). With at least 38 eruptions in the past 200 yr, it is one of the most active volcanoes in the Aleutian arc. Pavlof lava is an advantageous composition to use in these experiments because quasi-steady magma supply rates, short magma-residence times, and limited interaction with host rocks preserve compositions of magmas ascending from deep-crustal storage.

Lava sample 03S75M1 of Mangan et al. (2009) was used in experiments. The flow from which the sample was extracted is mildly vesicular (7 vol%) and hosts sub-millimeter phenocrysts composed of ~10 vol% plagioclase (An_{60-70s}), 5 vol% augite + hypersthene, and 1 vol% olivine (Fo_{70s}). Antecrysts of anorthitic plagioclase of millimeter size are randomly scattered through the flow. The bulk composition of the starting material is listed in Table 1.

Rock powder previously prepared for XRF analysis was reground by hand in agate under triple-distilled water to a non-gritty talcum powder-like feel (generally less than 10 μm), then dried and stored in a laboratory oven at 110 °C. To improve precision of H_2O additions and to avoid loss of water during welding, this nominally anhydrous rock powder was mixed with ground, previously hydrated glass created from the same sample. Hydrous glass "spikes" were produced by loading and welding shut 5 mm diameter Au capsules filled with 92 wt% nominally dry rock powder and 8 wt% triple-distilled water (200 mg total weight). The sealed capsules were held at 1050 °C at 1200 MPa in a piston-cylinder apparatus for 5–8 h before rapid quenching to bubble-free glass. The resulting hydrous glass spike was ground and added to the dried nominally anhydrous rock powder to obtain the desired initial component of H_2O. The CO_2 was added to the mixed dry + hydrous powders as Ag oxalate proportioned to deliver a consistent 1 wt% CO_2 to the starting mix.

The experiments were conducted using a modified double-capsule configuration in which 40 mg of starting material comprising a mix of nominally dry rock powder and the hydrous glass spike in proportions intended to deliver 2, 4, or 6 wt% H_2O depending on the run. The mixed starting powder and 1.5 mg Ag oxalate were packed into a 3 mm diameter $Ag_{70}Pd_{30}$ capsule snugly sheathed in thin-walled Pt tubing to prevent physical contact of the inner capsule with the Ni-NiO buffer used to regulate oxygen fugacity. The sheathed capsule was welded shut at one end using a graphite arc welder. Once filled, the open end of the sheathed capsule was then crimped, the previously sealed lower end placed in an ice bath, and the open end closed by arc welding.

Table 1. Composition of starting material

Oxide	wt%
SiO_2	52.6
TiO_2	1.22
Al_2O_3	18.4
FeO_{total}	9.67
MnO	0.20
MgO	4.72
CaO	8.93
Na_2O	3.40
K_2O	0.62
P_2O_5	0.29

Notes: Bulk composition in wt% oxides by XRF for Pavlof lava sample 03S75M1 in Mangan et al. (2009); FeO_{total} is all iron reported as FeO, and the analysis is normalized to 100 wt% volatile-free.

Each inner capsule was tested for leaks by weighing, heating, and re-weighing. Sealed sample capsules were then placed in a 5 mm diameter, Pt outer capsule packed with 190 mg of a 1:1 (wt.) Ni-NiO buffer and 5 mg of a C-O-H source. The C-O-H source was added to the outer capsule to fix the f_{H_2} in the inner capsule by diffusion, and through this control, the sample f_{O_2} by reproducing mole fractions of H_2O and CO_2 in the buffer fluid to match the anticipated mole fractions of H_2O and CO_2 of the fluid inside the sample capsule at equilibrium. The anticipated fluid composition in equilibrium with the melt was estimated from the solubility model of Papale et al. (2006) for specific run conditions. The C-O-H buffer added to the outer capsule was either a mix of Ag oxalate plus anhydrous oxalic acid or was pure oxalic acid di-hydrate, as shown in Table 2.

The expected yields of CO_2 released by decarbonation of Ag oxalate, anhydrous oxalic acid, and oxalic acid di-hydrate were confirmed by loading and welding those components into flattened Pt capsules. The sealed capsules were weighed and then heated with a propane-air flame until they expanded, indicating thermal decomposition of their contents. Upon cooling to room temperature, the capsules were re-weighed, those that leaked were discarded, and sealed capsules were placed in a freezer overnight to condense and freeze H_2O. Upon removal from the freezer, the exterior of each capsule was wiped dry to remove condensation and punctured to release the evolved CO_2 gas. The capsule was then re-weighed to determine weight percent CO_2 lost and then placed in a 110 °C oven to vaporize and release the H_2O component of the decarbonation reaction. Finally, the capsule was removed from the oven and re-weighed. The mass balances showed the CO_2 liberated during decarbonation of Ag oxalate was within 4% of the expected stochiometric yield; the CO_2/H_2O yield for oxalic acid di-hydrate was within 2% of the expected stochiometric yield; and decarbonation of anhydrous oxalic acid liberated CO_2 gas within 7% of the expected stochiometric yield.

We chose an above-liquidus run temperature of 1125 °C; lower temperature runs at 1050 and 1100 °C crystallized stable pyroxene and plagioclase or produced glasses with quench crystals. Isothermal experiments at 310–1200 MPa were conducted in a one-inch, end-loaded, solid-media, piston-cylinder apparatus with a graphite furnace and pressed-CaF_2 assembly (e.g., Sisson et al. 2005; Blatter et al. 2013). The hydraulic line of the piston cylinder was linked to an argon gas reservoir permitting small, precise adjustments to pressure during equilibration and controlled pressure release during decompression runs (Lautze et al. 2010). While the runs were intended to be at even 100 MPa values, subsequent refinement of the pressure calibration using the CsCl melting technique (Bohlen 1984) led to the recalculated final pressure values reported in our results.

In both solubility and decompression experiments, capsules were aligned perpendicular to the long axis of the furnace bore and positioned in the predetermined thermal maximum. The temperature gradient across the capsule was <6 °C. Temperature was controlled using an S-type thermocouple ($Pt\text{-}Pt_{90}Rh_{10}$) positioned at the medial axis of the capsule. Run temperatures varied by <1 °C during the experiments. Pressure was calibrated by bracketing the melting curve of thoroughly dried CsCl to within ±2.5 MPa at 400, 800, and 1200 MPa after Bohlen (1984). Overnight variations in room temperature led to minor pressure changes (≤10 MPa) during runs that were adjusted such that runs were at their reported pressures for at least several hours before quenching.

Runs were equilibrated at temperature and pressure for 24 ± 1 h. Solubility experiments were quenched immediately after equilibration. Decompression experiments underwent controlled pressure reduction (120–160 MPa/s) after equilibration at the initial pressure and then held a final pressure for a time of <1 to 3750 s depending

Table 2. Fluid buffers

Fluid buffer no.	Volatiles added to inner capsule (wt%)	Anticipated CO_2:H_2O for fluid in equilibrium with melt (molar)	Volatile buffer added to outer capsule (wt%)
1	2% H_2O + 1% CO_2	80:20:00	87%$Ag_2{\cdot}2(CO_2)$ + 13% $C_2H_2O_4$
2	4% H_2O + 1% CO_2	70:30:00	66% $Ag_2{\cdot}2(CO_2)$ + 34% $C_2H_2O_4$
3	6% H_2O + 1% CO_2	60:40:00	100% $C_2H_2O_4{\cdot}2(H_2O)$

Notes: One of three fluid buffers were added to the outer capsules. The buffer selected for each run matched the anticipated equilibrated fluid composition as calculated by the solubility model of Papale et al. (2006) for 2, 4, or 6 wt% H_2O and 1 wt% CO_2 added to inner capsule.

on the run. In both types of experiments, rapid quenching was accomplished by abruptly turning off current to the furnace. The measured quench rate for the piston cylinder is a decrease of 40–70 °C/s (Bista et al. 2015). Each capsule was punctured and examined with a binocular microscope to assure that the Ni-NiO buffer was not exhausted during the run and that the fluid buffer was present.

We note here that additional carbon can be unintentionally introduced to runs in detectable amounts via diverse mechanisms such as non-stochiometric yields of Ag oxalate, capsule welding, the piston cylinder's graphite furnace assembly, trace organic contaminants in the rock powder, and possible metal-drawing compounds trapped during tubing manufacturing. For example, using the same experimental equipment, Blatter et al. (2013) report incorporation of 650 ± 70 ppm CO_2 in hydrous basalt during rapid fusion (10 min) experiments conducted at 900 MPa and 1350 °C using $Au_{75}Pd_{25}$ capsules. In addition to the potential for absorption of atmospheric water; high-temperature experiments are also subject to unintentional H_2O additions from the reduction of ferric into ferrous iron (Holloway et al. 1992). Lesne et al. (2011) report unintentional hydration of alkali basalt melts ranging non-systematically between 0.7–1.3 wt% H_2O in CO_2-solubility experiments conducted at 1200 °C and 20–200 MPa (Pt capsules; 4–8 h run duration; internally heated pressure vessel). In this study, blank experiments (Pavlof powder without added Ag oxalate or water) were run to evaluate such artifacts. Nominally dry rock powders (stored at 110 °C) were encapsulated in Pt and held at 1250 °C and 885 MPa for 10 min and then quenched to glass. We find that unintentional volatile additions may reach 0.8–1.1 wt% H_2O and 1100–1120 ppm CO_2 in our experiments (see Results section).

Compositional determinations

Major-element compositions of run glasses were determined using the USGS JEOL 8900 electron microprobe in Menlo Park, California, operated at an accelerating voltage of 15 kV. Alkali loss was minimized using a 2 nA beam current, a 10 µm spot, and a 10 s counting time for Na. A variety of natural and synthetic minerals, including basaltic glass VG-A99 (Jarosewich et al. 1980) were used as standards, and background-corrected count rates were converted to concentration with the JEOL proprietary version of the CITZAF reduction routine (Armstrong 1995). Glass analyses involved regularly spaced traverses along and across the capsule length to test for glass homogeneity.

High-temperature, vacuum-extraction manometric measurements of dissolved H_2O and CO_2 were made at the University of Lausanne, Institute of Mineralogy and Geochemistry, Lausanne, Switzerland. Hydrogen and carbon concentrations (reported as wt% H_2O and CO_2) were analyzed in glasses from four basaltic andesite experiments equilibrated at 1015, 880, 815, and 520 MPa with 1 wt% added CO_2 and 1 or 4 wt% added H_2O. These melts coexisted with excess H_2O-CO_2 fluid, but glass splits selected for analysis were visibly bubble-free. The method used, modified from Vennemann and O'Neil (1993), included transferring crushed, cleaned, and weighed glass powders to silica tubes. Each sample was covered with previously outgassed quartz grains and silica wool and then held at 10^{-6} mbar at 50 °C for at least 12 h to remove surface H_2O. Samples were then heated to temperatures in excess of 1400 °C using an oxygen-propane torch until no further gas was released. Released volatiles were condensed in a liquid nitrogen trap (–196 °C). Non-condensable volatiles, including any reduced H or C species, were oxidized by CuO (at 700 °C). H_2O and CO_2 were subsequently separated using ethanol-liquid nitrogen slush traps (held at about –85 °C). The total CO_2 was then measured using a calibrated electronic manometer. The H_2O was transferred and sealed into a glass tube that contained Zn metal and was heated to 500 °C to produce H_2 for subsequent measurement using a Finnigan MAT 253 mass spectrometer. Weighed amounts of H_2O were always run in parallel with the samples to correct for daily variations in the tuning and sensitivity of the mass spectrometer. Although measurements were not replicated for individual samples, experience in the laboratory indicates uncertainties of about 2% of measured concentrations for H_2O and 5% of measured concentrations for CO_2.

Ion microprobe analyses were obtained for dissolved H_2O and CO_2 using the Cameca 1280 ion mass spectrometer (IMS) at the Northeast National Ion Probe Facility at Woods Hole Oceanographic Institution, Woods Hole, Massachusetts. Polished slices of the experimental glasses were mounted in an indium substrate to reduce carbon and hydrogen backgrounds. Analytical conditions include Cs+ primary beam ~10 µm in diameter at 10 kV accelerating voltage and 1–2 nA of beam current, 30 × 30 raster size (µm), 4 min pre-sputtering, and 20 cycle data. Measurements on our internal standards (glass splits from run products analyzed by manometry), combined with in-house subaerially degassed mafic glasses, provided working curves for calculation of H_2O and CO_2 concentrations in our unknowns.

Volatile concentration measurements were also attempted on a few glasses by Fourier-transform infrared spectroscopy at the USGS Volatile Laboratory in Menlo Park, California. The lab has a Nicolet Magna 750 FTIR with a SpectraTech Analytical-IR microscope attachment containing a liquid-nitrogen-cooled MCT-A detector. Spectra were acquired on 100 µm spots from 512 scans collected at 4 cm^{-1} resolution between 500 and 4000 cm^{-1}. Dissolved water concentrations were calculated with Beer's Law (Dixon et al. 1995) using the H_2O_{total} peak (3530 cm^{-1}) with an extinction coefficient of 63 l/mol-cm (Dixon et al. 1995), but many samples could not be thinned sufficiently to avoid detector saturation. Carbon dioxide concentrations were calculated using the $CO_3^=$ doublet peaks (1515 and 1430 cm^{-1}) with an extinction coefficient of 375 l/mol-cm based on basalt glass (Fine and Stolper 1986). As other researchers have noted, precise, but not necessarily accurate, baselines can be fitted to $CO_3^=$ doublets. We followed the curved-baseline methods described in King and Holloway (2002) to estimate maximum and minimum concentration for each doublet and report the average of the two as CO_2 in our data tables. A glass density of 2640 kg/m^3 was determined from glass composition and used in our calculations. Agreement can be poor between CO_2 concentrations measured by manometrically calibrated IMS and by FTIR, pointing to the aforementioned difficulties defining accurate FTIR backgrounds in the carbonate region.

Attempts were made to extract and measure the composition of the gas/fluid phase in equilibrium with the melt using inductively coupled plasma mass spectrometry (micro-ICPMS), but these efforts failed to produce reproducible results due to the small amount of excess vapor present at the end of our runs. Masses of quenched excess fluid were not measured, due to the difficulty of cleaning inner capsules of buffer and the likelihood of fluid trapped in vesicles along capsule walls, but rough values from mass-balance indicate low quantities, generally ≤1 mg and certainly <2 mg. Calculations of fluid composition by mass-balance also proved of insufficient precision due to the aforementioned uncertainties in total H_2O and CO_2 concentrations. The mass-balance approach propagates analytical, weighing, and other uncertainties onto the fluid's apparent composition, and these are magnified by the fluid's low mass fraction. In lieu of direct measurement, the mole fraction of CO_2 in the coexisting fluid phase was estimated building on the approach of Iacono-Marziano et al. (2012), in which the fluid is treated as a binary mixture of H_2O and CO_2 for which total pressure (LHS in Eq. 1) is the sum of the partial pressures of the mixed fluid (RHS in Eq. 1) with the partial pressure of CO_2 in the mixed fluid converted to mole fraction as in Equation 2:

$$P_{total} = P_{H2O}^{mixed\ fluid} + P_{CO2}^{mixed\ fluid} \quad (1)$$

$$X_{CO2}^{mixed\ fluid} = P_{CO2}/P_{total}. \quad (2)$$

The CO_2 fugacity (f_{CO_2}) can then be calculated from the fluid bulk composition, temperature, and total pressure using an appropriate mixed-fluid equation of state.

The partial pressure of H_2O in the mixed fluid ($P_{H2O}^{mixed\ fluid}$) is approximated by applying a solubility model to derive the mole fraction of H_2O in a mixed H_2O-CO_2 fluid that would yield the dissolved H_2O concentration measured in our experimental melts at each synthesis temperature and total pressure. This approach assumes that: (1) the effects of melt composition, pressure, and temperature on H_2O solubility are adequately known, and (2) dissolved CO_2 is of insufficient abundance in the melt to influence dissolved H_2O at high pressure as per Ni and Keppler (2013). The solubility models of Ghiorso and Gualda (2015) and of Papale et al. (2006) were applied to derive two estimates of $X_{H2O}^{mixed\ fluid}$ and $X_{CO2}^{mixed\ fluid}$, and from these, $P_{H2O}^{mixed\ fluid}$ and $P_{CO2}^{mixed\ fluid}$, then f_{CO_2}, in both cases with ferric and ferrous iron in the melt set for an f_{O2} of Ni-NiO at 1125 °C (Kress and Carmichael 1988).

The practical approach was to enter the Pavlof melt composition into the software-application version of those solubility models, then adjust the H_2O and CO_2 concentration values so that the melt would be saturated at each run's synthesis temperature and total pressure with a trace (≤0.1 wt%) of H_2O-CO_2 fluid, with the melt's predicted dissolved H_2O concentration matching that measured in each glass. The dissolved CO_2 concentrations predicted by the models at those conditions were not required to match measured values since CO_2 solubility was the aspect potentially requiring revision. Both solubility models employ non-ideal equations of state for the fluid to derive H_2O and CO_2 fugacities, but the software applications of those models report the saturating fluid's estimated composition ($X_{CO2}^{mixed\ fluid}$, $X_{H2O}^{mixed\ fluid}$), not those underlying fugacities. The fluid compositions reported by the two saturation models were therefore used to calculate two estimates of CO_2 fugacity for each run at its synthesis conditions using the non-ideal mixed fluid fugacity model of Churakov and Gottschalk (2003a, 2003b) (at http://fluid-eos.web.psi.ch/EOS/calculator_simple.html). Spot comparisons show close agreement of the obtained f_{CO_2} with values derived with the CORK H_2O-CO_2 fluid model of Holland and Powell (1991, 2003), and the Allison et al. (2019) MATLAB calculator that employs a modified Redlich-Kwong equation of state corrected for high pressure after Saxena and Fei (1987). The Papale et al. (2006) solubility model is calibrated to 1000 MPa, so for higher run pressures, the partial pressure of H_2O necessary at 1000 MPa to yield the measured dissolved H_2O concentration was applied as the H_2O partial pressure at the higher total run pressure. Both solubil-

ity models treat the saturating fluid as a non-ideal binary mix of H_2O and CO_2, so effects of $X_{CO_2}^{mixed\ fluid}$ on f_{H_2O} are addressed internal to those models. A simpler approach for estimating f_{CO_2}, more similar to that of Lesne et al. (2011), was initially employed involving determining the total pressure at which each run would attain its measured dissolved H_2O concentration if saturated with pure H_2O, with that pressure then used as the H_2O partial pressure at run conditions, with $P_{CO_2}^{mixed\ fluid}$ and $X_{CO_2}^{mixed\ fluid}$ determined as in Equations 1 and 2. That approach does not, however, capture the increasingly non-ideal behavior of the mixed fluid with increasing pressure, leading to underestimates of f_{CO_2} to about 20% relative that increase systematically with pressure, and so was abandoned. Differences in f_{CO_2} derived applying the Ghiorso and Gualda (2015) vs. the Papale et al. (2006) models for H_2O solubility range from 4–20% of their mean (average of 10.1%, median of 8.9%). Applying the Papale et al. (2006) model consistently yields greater f_{CO_2} values, with the difference generally increasing with dissolved H_2O concentrations, reflecting a lower $P_{H_2O}^{mixed\ fluid}$ required by that model to achieve a specific dissolved H_2O concentration.

Results

General characteristics of the glasses

The major-element compositions of the quenched glasses are within the analytical uncertainty of the whole-rock XRF analysis of the starting material (cf. Tables 1 and 3) except FeO_{total}, which is ~0.5 wt% lower in run products. All glasses are translucent brown and crystal-free. Solubility runs produced bubble-free glass, with a few minute scallops at the capsule wall where excess gas/fluid pooled during the run. Rapid decompression followed by immediate quench produced glass with sparse, difficult-to-discern bubble embryos (no. 1916), and at increasing dwell times at P_{final}, vesiculated glass with textures suggesting an initially uniform distribution of bubbles (run no. 1919) that then segregated toward the top of the capsule (no. 1958, no. 1962). Number densities measured in bubble segregations (foam) decline with increasing hold times due to coalescence and ripening (see Lautze et al. 2010). Textures produced during decompression runs are described in Table 4 and illustrated in Figure 1.

Table 3. Major element composition (wt%) of experimental glasses

Run no.	1892	1890	1894	Average glass
Run pressure	330 MPa	533 MPa	884 MPa	composition
SiO_2	52.9 ± 0.2	53.0 ± 0.2	53.1 ± 0.3	53.0 ± 0.1
TiO_2	1.22 ± 0.10	1.15 ± 0.07	1.14 ± 0.11	1.17 ± 0.05
Al_2O_3	18.8 ± 0.1	19.0 ± 0.1	19.0 ± 0.2	18.9 ± 0.1
FeO_{total}	9.21 ± 0.14	8.82 ± 0.17	8.84 ± 0.19	8.96 ± 0.22
MnO	0.23 ± 0.05	0.30 ± 0.05	0.31 ± 0.07	0.28 ± 0.04
MgO	4.49 ± 0.05	4.53 ± 0.07	4.47 ± 0.06	4.50 ± 0.03
CaO	8.99 ± 0.10	8.98 ± 0.11	8.86 ± 0.09	8.94 ± 0.07
Na_2O	3.48 ± 0.11	3.55 ± 0.13	3.62 ± 0.08	3.54 ± 0.07
K_2O	0.61 ± 0.03	0.60 ± 0.03	0.60 ± 0.03	0.60 ± 0.01
SO_3	0.01 ± 0.01	0.02 ± 0.01	0.01 ± 0.01	0.01 ± 0.01
Cl	0.04 ± 0.01	0.03 ± 0.01	0.04 ± 0.01	0.04 ± 0.0
Original sum	96.0 ± 0.3	95.1 ± 0.4	95.7 ± 0.4	95.6 ± 0.4

Notes: Glass analyses by electron microprobe. Standard deviations of multiple analysis points are reported as ± wt%. Compositions were normalized to 100 wt%; original summations are reported in the final row. Equilibration pressure for each run is given in the second row. All three runs equilibrated with 2 wt% H_2O and 1 wt% CO_2 added to the inner capsule; outer capsules contained buffer composition no. 1.

Volatile components and concentrations

Glasses from several experiments were analyzed via FTIR to determine the molecular form of the volatiles dissolved in the glass. For some samples, well-defined peaks were observed for H_2O_{total} (3500 cm^{-1}), $H_2O_{molecular}$ (5200 cm^{-1}), and OH^- (4519 cm^{-1}). Relative peak heights suggest ≥62% of the water dissolved in the melt was in the form of OH^- at the point speciation was locked during quenching. Dissolved carbon in quenched glass manifests as $CO_3^=$ doublets (1500 and 1422 cm^{-1}), with symmetries and peak-to-peak distances constant across a range of experimental pressures and volatiles. A minor CO_2 absorbance peak (2350 cm^{-1}) occurs in several spectra, but in all cases would constitute ≤1.3% of the total dissolved carbon, and contamination of the measurements by atmospheric CO_2 cannot be excluded. An example of a well-resolved spectrum is given in Figure 2.

Concentrations of dissolved H_2O and CO_2 were estimated from FTIR spectra for a handful of experimental glasses, but our primary data set, provided in Table 5, comes from ion microprobe measurements calibrated on Pavlof reference glasses measured by manometry.

In some run glasses, excess dissolved H_2O and/or CO_2 is indicated; that is, the dissolved volatile concentration measured in the glass by ion probe exceeds that originally added to the capsule. Although unintentional presence of H_2O and CO_2 is indicated by our blank experiments (runs no. 1903A and no. 1913A in Table 5), we cannot rule out another possibility that C and H from the fluid buffer infiltrated the inner capsule. The ease of C and H diffusion through Pt capsules (and Pd) is well known (e.g., Brooker et al. 1998); high-pressure infiltration through Ag-Pd alloys is expected to be slower, but exact rates are unknown.

Data from Table 5 are plotted in Figures 3, 4, 5, and 6. Measured concentrations of dissolved H_2O and CO_2 for each pressure (Fig. 3) resemble saturation isobars familiar from other solubility studies, with nearly constant to weakly declining CO_2 concentrations with increasing dissolved H_2O over the range of H_2O concentrations investigated. Ni and Keppler (2013) reviewed results from the limited number of C-O-H solubility experiments published for mafic melts at high pressure and made a similar observation, noting that at pressures ≥500 MPa "CO_2 solubility is nearly constant (within uncertainties) over a broad H_2O concentration range (~1–5 wt% H_2O)." Figure 4 shows dissolved CO_2 concentrations plotted vs. total pressure, dissolved H_2O concentrations plotted vs. estimated $P_{H_2O}^{fluid}$, and dissolved CO_2 concentrations plotted vs. estimated $P_{CO_2}^{fluid}$. Values for $P_{H_2O}^{fluid}$ and $P_{CO_2}^{fluid}$ are simply $P_{total} \times X_{H_2O}^{mixed\ fluid}$ and $P_{total} \times X_{CO_2}^{mixed\ fluid}$ and are plotted as the mid-points and ranges of the fluid compositions derived with the Papale et al. (2006) and Ghiorso and Gualda (2015) solubility models. Dissolved H_2O concentrations increase at close to the canonical square root of P_{H_2O} relation long known from experimental studies for fluid-saturated melts at low

Table 4. Decompression results

Run no.	Dwell time (s)	Porosity (vol%)	Bubble diameter (mm)	Bubble number density (bubbles/mm^3)	Glass texture
1916	<1	<1	≤0.001	$\leq 1\times10^0$	Sparse, ghostly bubble embryos
1919	30	5.0 ± 0.5	0.01 ± 0.001	$1.5\times10^4 \pm 6\times10^3$	Uniform bubble distribution
1958	150	4.5 ± 0.6	0.02 ± 0.003	$1.3\times10^3 \pm 3\times10^1$	Non-uniform distribution; lower bubble-poor zone
1962	3750	5.1 ± 0.3	0.009 ± 0.002	$2.3\times10^2 \pm 1\times10^2$	Non-uniform distribution; upper foam layer

Notes: After equilibration at 1040 MPa, runs were rapidly decompressed to 310 MPa and then held for various dwell times prior to quenching. The ± values represent standard deviation of multiple measurements of glass porosity, bubble diameter, and bubble number density; values for non-uniform distributions represent bubble-rich areas in upper part of capsule.

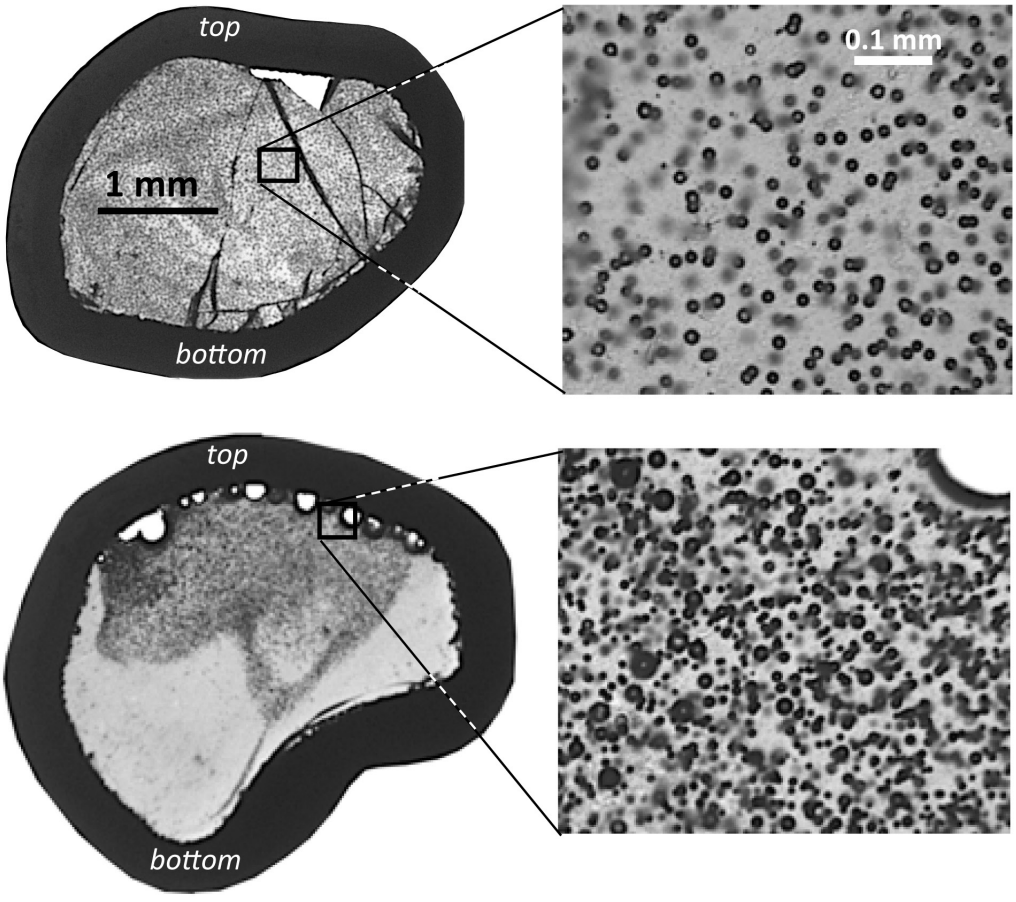

Figure 1. Photomicrographs of decompression glasses. Cross sections through capsules are on the left with corresponding close-up images shown on the right. The upper pair of images shows uniform bubble size and distribution (run no. 1919); bubbles in the lower pair of images (no. 1962) are heterogeneous in size and distribution due to coalescence and segregation over longer dwell times at P_{final} (30 s vs. 3750 s for no. 1919 and no. 1962, respectively). Left and right scale bars apply to top and bottom images.

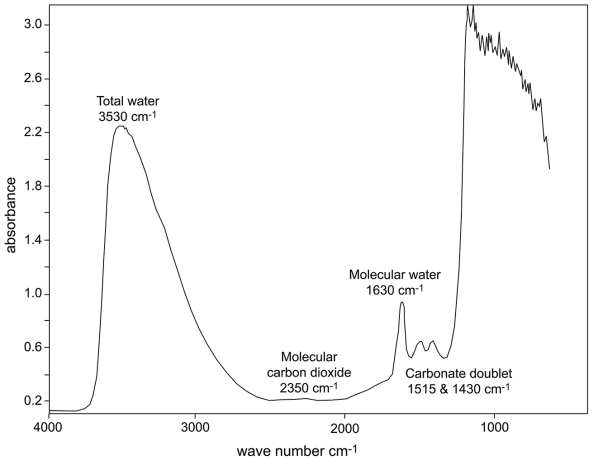

Figure 2. FTIR spectrum of quenched glass from run no. 1910. Sample thickness was 28 μm. Absorbance is equal to the logarithm of the measured IR signal through the reference spectrum (air) divided by the sample spectrum (air plus sample).

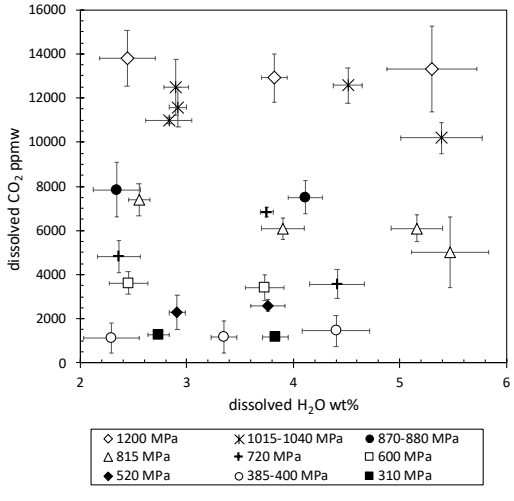

Figure 3. Concentrations of dissolved CO_2 (ppmw) vs. dissolved H_2O (wt%) for solubility experiments conducted at 1125 °C and total pressures of 310–1200 MPa in basaltic andesite melt. Error bars are 2-σ uncertainties. Results are subdivided by total run pressure.

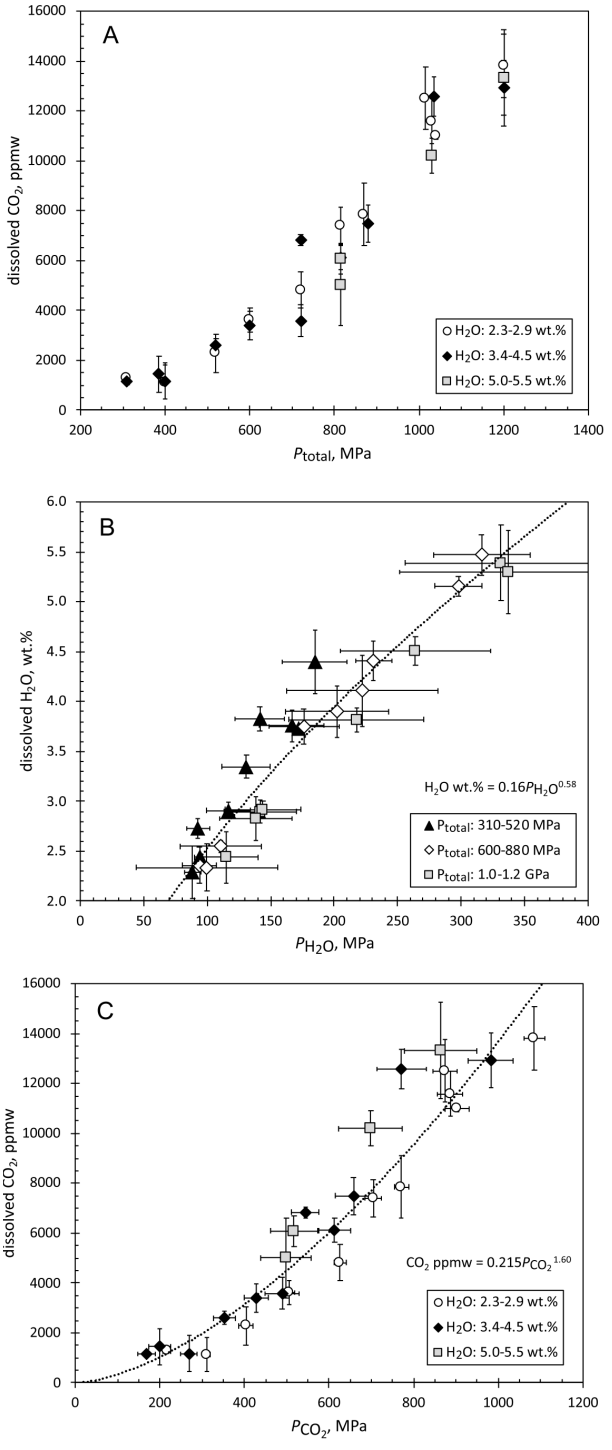

►**Figure 4.** (**a**) Experimental total pressure (P_{total}) plotted against dissolved CO_2 concentrations (ppmw) in experimental glasses measured by ion microprobe, with 2-σ concentration uncertainties (some error bars are smaller than data symbol). Glasses are subdivided by dissolved H_2O concentrations. (**b**) Calculated H_2O pressure (P_{H_2O}) in the fluid plotted against dissolved H_2O concentration (wt%) in glasses measured by ion microprobe, with 2-σ concentration uncertainties. Glasses are subdivided by run pressure. (**c**) Calculated CO_2 pressure (P_{CO_2}) in the fluid plotted against dissolved CO_2 concentration (ppmw) in glasses measured by ion microprobe, with 2-σ concentration uncertainties. Glasses are subdivided by dissolved H_2O concentrations. Plotted H_2O and CO_2 fluid-pressure values in **b** and **c** are mid-points of derivations from Ghiorso and Gualda (2015) and Papale et al. (2006) H_2O solubility models, as described in text, with uncertainty bars showing solution ranges; dotted lines in **b** and **c** are unweighted power-law regressions yielding the indicated equations, chiefly for reference.

pressure or with $X_{H_2O}^{fluid} < 0.5$ (Hamilton et al. 1964; Burnham 1979). Both the Ghiorso and Gualda (2015) and Papale et al. (2006) solubility models require slightly greater $P_{H_2O}^{fluid}$ at greater total pressure to attain the same dissolved H_2O concentration (Fig. 4b). Since $P_{CO_2}^{fluid}$ is estimated by difference and our higher H_2O melts were produced at greater total pressures (Table 5), this also appears as slightly lower $P_{CO_2}^{fluid}$ values to attain the same dissolved CO_2 concentrations in higher-H_2O melts (Fig. 4b).

Solubilities are more appropriately referenced to fugacities, with CO_2 fluid being strongly non-ideal at high pressures where $f_{CO_2} >> P_{CO_2}^{fluid}$. Fugacities can be expressed as in Equation 3:

$$f_{CO_2} = \gamma_{CO_2} \times P_{CO_2}^{mixed\ fluid} \quad (3)$$

where γ_{CO_2} is the fugacity coefficient for CO_2, and similarly for H_2O, although in the present case fugacities were obtained directly from fluid composition and intensive conditions using the software application version of the Churakov and Gottschalk (2003a, 2003b) mixed fluid equation of state (at http://fluid-eos.web.psi.ch/EOS/calculator_simple.html) without the need of the intermediate step of deriving γ_{CO_2}. Figure 5 illustrates the relation between f_{CO_2} and total pressure, that the drier melts coexisted with drier fluids, and that all the fluids were relatively H_2O-poor. Figure 6 shows that dissolved CO_2 concentrations increase with increasing f_{CO_2} (Ghiorso and Gualda-based derivation) following a power-law relation that is robust to about f_{CO_2} = 14 000 MPa (total pressure greater than ~1000 MPa). Higher-pressure results plot farther from the regression line but remain within its propagated uncertainty envelope, and no strong association is apparent between dissolved H_2O concentrations and CO_2 solubility.

Implications

Comparing experiments and solubility models

In Figure 7 we compare our experimental data with results from three recent and conveniently available CO_2-H_2O solubility models: Papale et al. (2006), Iacono-Marziano et al. (2012), and Ghiorso and Gualda (2015). The thermodynamic model of Papale et al. (2006) evaluates the excess Gibbs free energy of coexisting melt + vapor with the melt phase treated as a non-isometric mixture of 8 major-element oxides, H_2O, and CO_2. The Iacono-Marziano et al. (2012) model is a semi-empirical formulation for the solubility of C-O-H fluids based on structural properties, with dissolved CO_2 concentrations determined by the number of non-bridging oxygen per oxygen (NBO/O) and the type of charge balancing cations present in the melt, with the relative positive influence of Na^+, $K^+ > Ca^{++} >> Mg^{++}$ on dissolved CO_2. Ghiorso and Gualda (2015) incorporate H_2O and CO_2 solubility into the regular-solution model formalism of the MELTS thermodynamic software assemblage with the simplifications that dissolved H_2O

TABLE 5. Experimental starting conditions and results

Run no.	*P* (MPa)	+H_2O[a] (wt%)	+CO_2[a] (wt%)	Fluid buffer	wt% H_2O dissolved[b]	ppm CO_2 dissolved[b]	wt% H_2O dissolved[c]	ppm CO_2 dissolved[c]	wt% H_2O dissolved[d]	ppm CO_2 dissolved[d]
Blank experiments (1250 °C)										
1903	885	0	0	none	–	–	–	–	1.13 ± 0.33	1122 ± 434
1913	885	0	0	none	–	–	–	–	0.78 ± 0.50	1099 ± 149
Solubility experiments (1125 °C)										
1901	310	2	1	1	2.73 ± 0.05	1275 ± 27	–	–	2.94 ± 0.04	2119 ± 180
1910	310	4	1	2	3.83 ± 0.06	1168 ± 62	–	–	3.74 ± 0.35	2027 ± 306
2112	400	2	1	1	2.29 ± 0.13	1136 ± 340	–	–	–	–
2114	400	4	1	2	3.35 ± 0.06	1166 ± 363	–	–	–	–
2147	385	6	1	3	4.40 ± 0.16	1453 ± 360	–	–	–	–
2235	520	2	1	1	2.91 ± 0.04	2286 ± 392	–	–	–	–
2068	520	4	1	2	–	–	3.76 ± 0.08	2600 ± 130	–	–
2091	600	2	1	1	2.45 ± 0.09	3620 ± 251	–	–	–	–
2092	600	4	1	2	3.73 ± 0.09	3417 ± 284	–	–	–	–
1908	720	4	1	2	3.75 ± 0.03	6840 ± 106	–	–	5.7 ± 0.43	6615 ± 405
2110	720	2	1	1	2.36 ± 0.10	4825 ± 366	–	–	–	–
2228	720	4	1	2	4.41 ± 0.13	3585 ± 320	–	–	–	–
2151	815	6	1	3	5.16 ± 0.12	6098 ± 310	–	–	–	–
2066	815	2	1	1	–	–	2.55 ± 0.05	7400 ± 370	–	–
2090	815	4	1	2	3.90 ± 0.10	6105 ± 241	–	–	–	–
2233	815	6	1	3	5.47 ± 0.18	5006 ± 803	–	–	–	–
2070	880	4	1	2	–	–	4.11 ± 0.08	7500 ± 375	–	–
2115	870	2	1	1	2.34 ± 0.11	7852 ± 622	–	–	–	–
2065	1015	2	1	1	–	–	2.90 ± 0.06	12500 ± 625	–	–
1898	1040	2	1	1	2.83 ± 0.11	10986 ± 69	–	–	3.04 ± 0.05	8645 ± 800
2062	1030	2	1	1	2.92 ± 0.04	11581 ± 446	–	–	–	–
2229	1035	4	1	2	4.51 ± 0.07	12571 ± 395	–	–	–	–
2243	1030	6	1	3	5.39 ± 0.19	10192 ± 351	–	–	–	–
2088	1200	2	1	1	2.44 ± 0.13	13800 ± 642	–	–	–	–
2089	1200	4	1	2	3.82 ± 0.06	12916 ± 551	–	–	–	–
2131	1200	6	1	3	5.30 ± 0.21	13316 ± 963	–	–	–	–
Decompression experiments (1125 °C, 1040 to 310 MPa)[g]										
1916	g	2	1	1	–	–	–	–	2.8 ± 0.10	4003 ± 88
1919	g	2	1	1	1.37 ± 0.11	4893 ± 647	–	–	–	–
1958	g	2	1	1	2.67 ± 0.10	4452 ± 430	–	–	–	–
1962	g	2	1	1	2.03 ± 0.07	1922 ± 203	–	–	–	–

Notes: Fluid buffer types in Table 2. Blank experiments were without added volatiles or fluid buffers. Uncertainties are given as ± values. FTIR concentration uncertainties reflect variation within a single glass wafer (6 analysis areas per wafer); IMS uncertainties are point-to-point glass variability plus uncertainty in IMS calibration curves; manometry concentrations are reported with relative error from calibration of the technique (5% of H_2O and 2% of CO_2 determined). Mole fractions of CO_2 in fluid ($X_{CO_2}^{fluid}$) and fugacity of CO_2 (f_{CO_2}) are calculated for two different H_2O solubility models as per text. Dashes indicate values not determined.

[a] Amounts of H_2O (wt%) and CO_2 (ppm) added to Pavlof basaltic andesite.

[b] Measured in glass by IMS.

[c] Measured in glass by manometry

[d] Measured in glass by FTIR.

[e] Mole fraction CO_2 in fluid and CO_2 fugacity calculated with Ghiorso and Gualda (2015) H_2O solubility model.

[f] Mole fraction CO_2 in fluid and CO_2 fugacity calculated with Papale et al. (2006) H_2O solubility model.

[g] Equilibration at 1040 MPa followed by decompression to and quenching at 310 MPa.

(Table extends to next page)

is fully dissociated into hydroxyl units and that CO_2 dissolves as both molecular CO_2 and carbonate units, the latter associated solely with Ca as a $CaCO_3$ component. Ghiorso and Gualda (2015) recognize that dissolved carbonate is also associated with other elements (Na, K, Mg) but note that insufficient experiments have been performed to model their activities.

Results for the Papale et al. (2006), Iacono-Marziano et al. (2012), and Ghiorso and Gualda (2015) solubility models are shown in Figure 7 for a melt of Pavlof basaltic andesite composition with 2, 4, and 6 wt% dissolved H_2O. The Papale et al. (2006) and Iacono-Marziano et al. (2012) results are similar to each other, and both overestimate the solubility of CO_2 in Pavlof basaltic andesite melt across the entire investigated range of f_{CO_2}, whereas the Ghiorso and Gualda (2015) model matches the measured trend of CO_2 concentrations with f_{CO_2} up to about 5000 MPa but underestimates CO_2 concentrations at greater f_{CO_2} values. Disparities

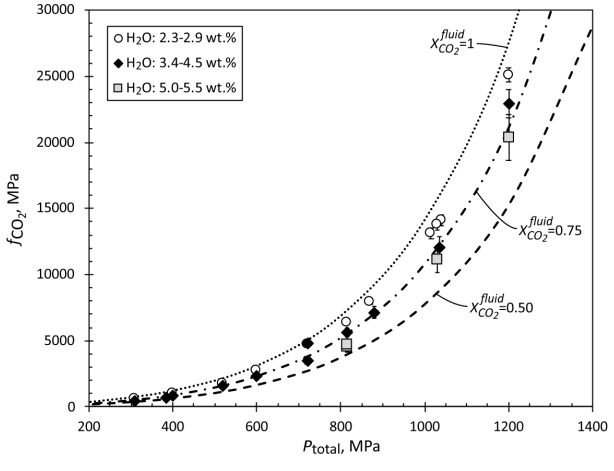

◀**FIGURE 5.** Experimental total pressure (P_{total}) plotted against CO_2 fugacity (f_{CO_2}) estimated as per text; symbols are plotted at the mid-points of f_{CO_2} values calculated using Ghiorso and Gualda (2015) and Papale et al. (2006) H_2O solubility models with error bars indicating solution ranges; glasses are subdivided by dissolved H_2O concentrations. Curves show f_{CO_2}–P_{total} relations of the Churakov and Gottschalk (2003a, 2003b) fluid equation of state applied to binary H_2O-CO_2 fluids at 1125 °C with the indicated mole fractions of CO_2.

TABLE 5.—*EXTENDED*

Run no.	$X_{CO_2}^{fluid}$[e]	$X_{CO_2}^{fluid}$[f]	f_{CO_2}(MPa)[e]	f_{CO_2}(MPa)[f]
Blank experiments (1250 °C)				
1903	–	–	–	–
1913	–	–	–	–
Solubility experiments (1125 °C)				
1901	0.68	0.74	510	550
1910	0.48	0.59	415	445
2112	0.80	0.83	975	1015
2114	0.63	0.72	820	935
2147	0.46	0.57	551	665
2235	0.74	0.81	1695	1835
2068	0.63	0.73	1480	1680
2091	0.82	0.87	2685	2825
2092	0.67	0.76	2230	2505
1908	0.72	0.79	3705	4025
2110	0.85	0.89	4650	4860
2228	0.62	0.74	3280	3785
2151	0.57	0.70	4135	4960
2066	0.84	0.89	6255	6575
2090	0.71	0.80	5345	5965
2233	0.54	0.69	4235	5180
2070	0.70	0.80	6735	7575
2115	0.87	0.90	7815	8145
2065	0.83	0.89	12750	13545
1898	0.84	0.89	13720	14540
2062	0.83	0.89	13370	14215
2229	0.69	0.80	11300	12900
2243	0.61	0.75	10135	12140
2088	0.88	0.93	24550	25645
2089	0.77	0.86	21825	24030
2131	0.65	0.79	18685	22080
Decompression experiments (1125 °C, 1040 to 310 MPa)[g]				
1916	–	–	–	–
1919	–	–	–	–
1958	–	–	–	–
1962	–	–	–	–

between the individual models, and with the Pavlof measurements, are likely due to the limited numbers of experimental solubility determinations upon which the models rest (Moore 2008; Ghiorso and Gualda 2015), particularly for higher pressures, and to the lack of studies that systematically vary concentrations of melt components that are likely to control CO_2 solubility, precluding adequately separating and characterizing their influences.

In detail, each solubility model can be displayed as a power-law relation between dissolved CO_2 and f_{CO_2}, and each such curve shifts to higher dissolved CO_2 concentrations at higher dissolved H_2O concentrations (Fig. 7). Shifts to higher dissolved CO_2 with higher dissolved H_2O (for a given f_{CO_2}) are larger in the models than is obvious from the Pavlof measurements, although such a shift is suggested by the highest f_{CO_2} Pavlof results. The cause of the model shift is twofold. Recent syntheses of CO_2-H_2O solubility in silicate melts (Papale et al. 2006; Iacono-Marziano et al. 2012; Ni and Keppler 2013; Duan 2014; Ghiorso and Gualda 2015) derive an enhancement of fluid-saturated melt CO_2 concentrations at low to intermediate melt H_2O concentrations, seen as an arching or doming of CO_2-H_2O concentration isobars (Fig. 8). Isobar doming becomes conspicuous at fluid-saturation pressures greater than about 500 MPa, with peak CO_2 concentrations also shifting to higher H_2O concentrations at greater fluid-saturation pressures. The second, subtle, but more general factor is that isopleths of constant f_{CO_2} have positive slopes across most of the relevant fluid-saturated CO_2-H_2O concentration space (CO_2: ordinate, H_2O: abscissa), such that they intersect higher-pressure saturation isobars at greater concentrations of both dissolved H_2O and CO_2 (Fig. 8). For a given f_{CO_2}, higher H_2O concentrations in the melt, therefore, require higher CO_2 concentrations and higher saturation pressures, irrespective of the presence or magnitude of H_2O-induced doming of saturation isobars. Enhancement of CO_2 solubility by addition of H_2O (isobar doming) is not obvious in the experimental H_2O and CO_2 concentrations of fluid saturated Pavlof basaltic andesite melt (Fig. 3), but a slight enhancement is suggested by relations between CO_2 concentration and $P_{CO_2}^{fluid}$ (Fig. 4c) and is allowed but not required by relations between CO_2 concentration and f_{CO_2} (Fig. 6). No experiments were conducted of the solubility of pure CO_2 fluid that would more clearly reveal a presence and magnitude of H_2O's ability to enhance CO_2 solubility, but our results do indicate that enhancements are less at high pressure than would be predicted by published H_2O-CO_2 solubility models (Fig. 7).

Presently, it appears that the most judicious approach to simulating degassing of mafic magmas ascending from the uppermost mantle into the lower- and mid-crust may be to employ a range of solubility models and accept the uncertainty that comes from their differences, instead of employing a single model that may allow precise calculations that, nevertheless, can be appreciably inaccurate.

Influence of melt composition on CO_2 dissolution

Although several experimental studies using mafic compositions demonstrate positive correlation between the CO_2 solubility and melt alkalinity, recent experiments by Allison et al. (2019) caution that the correlation is not a "simple scaling." Using the approach of Iacono-Marziano et al. (2012), we employ their

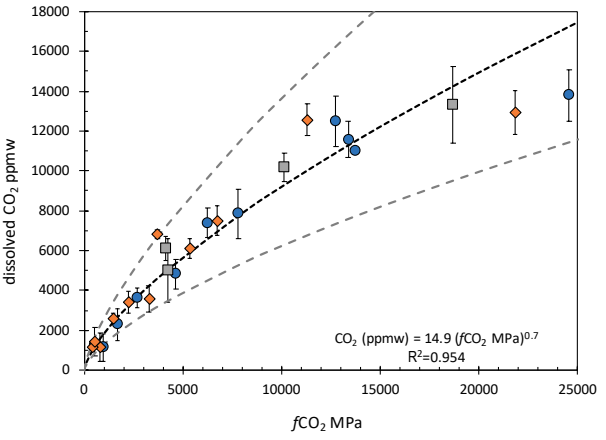

FIGURE 6. Calculated CO_2 fugacity vs. measured dissolved CO_2 concentrations for hydrous solubility experiments conducted at 1125 °C and total pressures of 310 to 1200 MPa (colored symbols, differentiated by dissolved H_2O as in Fig. 4). As per text, Ghiorso and Gualda (2015) H_2O solubility model was used to estimate of $X_{H_2O}^{fluid}$ and $P_{H_2O}^{fluid}$, and then by difference, $X_{CO_2}^{fluid}$, and $P_{CO_2}^{fluid}$ were calculated; subsequent f_{CO_2} values were obtained using Churakov and Gottschalk (2003a, 2003b). Vertical lines are 2-σ CO_2 concentration uncertainties for each data point (some error bars are smaller than data symbol). Dashed black line shows regression to all results: $\log_{10}CO_2(ppmw) = 1.1746(\pm0.1146) + 0.6976(\pm0.0314) \times \log_{10}f_{CO_2}(MPa)$ and ignores individual measurement uncertainties. Dashed gray lines propagate 1-standard error of the regression.

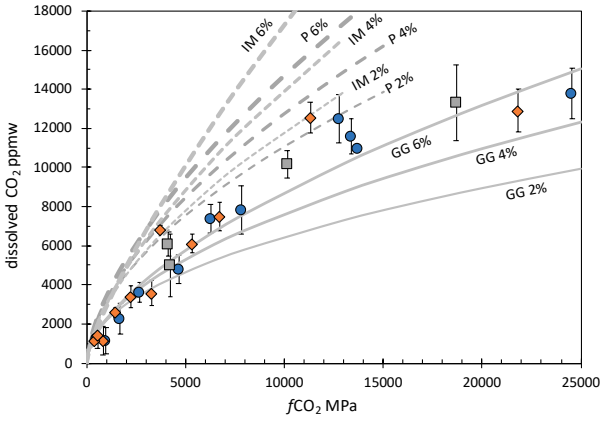

Figure 7. Comparison of Pavlof experiments (colored symbols, differentiated by dissolved H_2O as in Fig. 4) with solubility models of Papale et al. (2006) (long-dashed curves, P), Iacono-Marziano et al. (2012) (short-dashed curves, IM), and Ghiorso and Gualda (2015) (solid curves, GG). Model CO_2 solubilities were calculated for the Pavlof basaltic andesite composition as a melt with 2, 4, and 6 wt% dissolved H_2O at 1125 °C and 400, 600, 800, 1000 MPa (and 1200 MPa for the Ghiorso and Gualda model), the f_{CO_2} was determined from the H_2O and CO_2 mole fractions in the fluid at the model pressure as per Churakov and Gottschalk (2003a, 2003b), and fit to curves subdivided by H_2O concentrations denoted by 2, 4, and 6% on the curve labels.

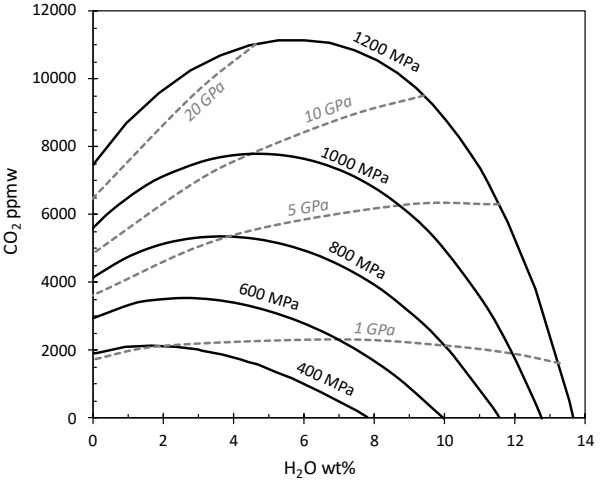

Figure 8. Synthetic H_2O-CO_2 concentration isobars (black lines) at indicated fluid saturation pressures (400–1200 MPa) for Pavlof basaltic andesite melt at 1125 °C and f_{O_2} of Ni-NiO, calculated with the Ghiorso and Gualda (2015) solubility model. Solubility models of Papale et al. (2006) and Iacono-Marziano et al. (2012) give similar-shaped results but that differ in detail. Isopleths of constant f_{CO_2} (dashed gray lines in GPa) are calculated from the saturated fluid compositions, temperature, and total pressure, using the mixed-fluid fugacity model of Churakov and Gottschalk (2003a, 2003b) through the web-based application at http://fluid-eos.web.psi.ch/EOS/calculator_simple.html.

"agpaitic index" [mole fraction (Na+K+Ca)/Al; *n.b.* agpaitic index is conventionally defined as molar (Na+K)/Al after Ussing (1912)] to examine a subset of our results in the context of previous high-pressure CO_2 solubility experiments for basaltic melts conducted under generally similar pressure-temperature-compositional conditions (Figs. 9 and 10).

The "agpaitic indices" labeled in Figure 9 correlate positively with CO_2 solubility. For a given f_{CO_2}, dissolved CO_2 is composition-dependent across a compositional spectrum of trachybasalt-alkali basalt-tholeiite-basaltic andesite. The correlation appears to hold at higher pressures as well, although the only experiments available for relevant comparison are a subset of Jakobsson (1997) for hydrous icelandite ("agpaitic index" 1.17) equilibrated at 1000 MPa total pressure and 1400 °C with 4.0–4.8 wt% dissolved H_2O (Fig. 10).

For basaltic melts, CO_2 solubility is largely insensitive to temperature (Ni and Keppler 2013), so differing synthesis temperatures should have little impact on the systematics displayed in Figures 9 and 10. The implication is that a relatively small shift in melt composition can lead to a significant difference in CO_2 solubility. At a fixed f_{CO_2} of 1000 MPa, for example, increasing the "agpaitic index" from 0.96 to 1.42 (Pavlof basaltic andesite to Etna trachybasalt) serves to increase the concentration of dissolved CO_2 by 190%. The primitive Aleutian basalt ID16 from Adak Island (Nye and Reid 1986) has "agpaitic index" of 0.88, similar to Pavlof basaltic andesite, so changes in CO_2 solubility may be small as parental arc basalts fractionate to basaltic andesites, but additional solubility studies systematically covering the spectrum of natural mafic melts are needed before deep CO_2-rich degassing can be modeled confidently.

Decompression, vesiculation, and re-equilibration

Although few, our near-instantaneous decompression experiments provide insight into melt re-equilibration following vesiculation at high degrees of CO_2 supersaturation. The glass produced in run no. 1919 records homogeneous nucleation of 10^4 bubbles/mm^3 for a dwell time of 30 s at P_{final} for a CO_2 supersaturation ratio of ~6 (measured concentration of CO_2 at P_{final}/equilibrium concentration at P_{final}). Runs no. 1958 and no. 1962 show the supersaturation ratio at quench decreases with increasing time at P_{final} from ~3 (150 s at P_{final}) to ~1 (3750 s at P_{final}), suggesting that the time required to re-establish equilibrium is somewhere between a few hundred to a few thousand seconds in our experiments.

The quasi-uniform distribution of bubbles in run no. 1919 makes it possible to estimate an effective diffusivity for CO_2 in hydrous basaltic andesite of 4.5×10^{-11} m^2/s. Our determination uses the expression given in Epel'baum et al. (1973)

$$D_{CO_2} = [\lambda^3\rho_m(\omega_o-\omega_f)/\rho_{CO_2}]^{2/3}{}_{\tau^{-1}} \quad (4)$$

in which λ is the mean distance between bubbles (~[number density]$^{-1/3}$ = 4×10^{-5} m), ρ_m is melt density (2600 kg/m^3 at 310 MPa, 1125 °C, and 1.37 wt% H_2O), ω_o, is the original weight fraction of dissolved CO_2 (0.0137 from run no. 2088), ω_f is the final weight fraction of dissolved CO_2 at quench (0.0049 from Table 5), ρ_{CO_2} is the fractional density of CO_2 dissolved in the melt (~10 kg/m^3 assuming partial molar volume of CO_2 of 3.3×10^{-5} m^3/mol) and τ is the diffusion duration, timed from the start of decompression to quench (62 s). Our empirical determination is consistent with that obtained using the argon proxy formulation in Zhang and

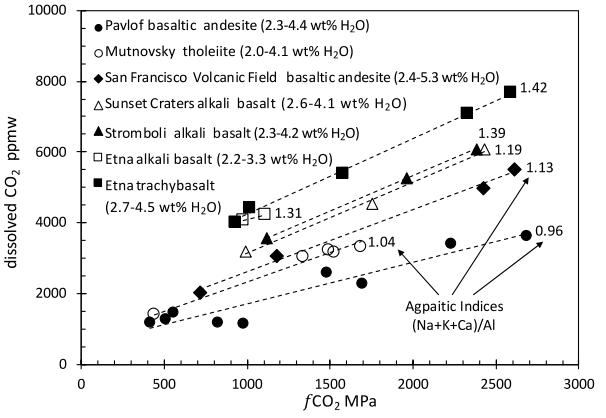

Figure 9. Comparison of CO_2 concentrations in hydrous basaltic melts experimentally equilibrated with a CO_2-rich gas/fluid phase ($X_{CO_2}^{fluid}$ = 0.46–0.93) covering experimental f_{CO_2} between 350–2685 MPa (300–610 MPa total pressure) and 1125–1250 °C. Range of dissolved H_2O for each experimental suite is given in parentheses. Data for Mutnovsky tholeiite is from Shishkina et al. (2010); Etna alkali basalt from Iacono-Marziano et al. (2012); other compositions (with the exception of our Pavlof basaltic andesite) are from Allison et al. (2019). The f_{O_2} conditions for all experiments were near Ni-NiO, with the exception of Iacono-Marziano et al. (2012) in which f_{O_2} is reported only as ">FMQ+1." For internal consistency, all f_{CO_2} values were calculated using the model of Churakov and Gottschalk (2003a, 2003b) using values of temperature, total pressure, and the fluid's mole fraction CO_2 as reported by the authors. Dashed lines are linear fits to the data. To the right of the trendlines, "agpaitic indices" [molar (Na+K+Ca)/Al] are given for each melt composition.

Ni (2010) for total effective binary diffusivity of CO_2, which gives 1×10^{-11} m^2/s using pressure-temperature-compositional conditions consistent with our experiments.

The peak bubble number density given in Table 4 is similar in magnitude to those reported for natural samples of scoria ejected during dry (and wet) basaltic Plinian eruptions (see summary in Mangan et al. 2014; Mastin 1997; Mastin et al. 2004; Polacci et al. 2006; Sable et al. 2006; Costantini et al. 2009, 2010). While it is tempting to equate the high bubble number density in our experiments to explosive, disequilibrium degassing of CO_2 as a trigger for Plinian basaltic eruptions, saturation depths of >15 km and rapid re-equilibration make this an unlikely scenario. For basaltic melts, Bottinga and Javoy (1991) show that a high-supersaturation ratio (≥3) is required for bubble nucleation in the shallow crust because the surface area of incipient bubbles is relatively large at low pressure, whereas for the higher pressure conditions of the lower- to mid-crust, the surface areas of incipient bubbles are smaller and the supersaturation ratio needed for nucleation is low; bubbles nucleate readily in the lower- to mid-crust, and rapid re-equilibration follows suit (see review in Mangan et al. 2014). Several petrologic studies suggest that magmas in the deep-crustal roots of many volcanic systems are saturated with a free, CO_2-rich fluid phase (see review in Lowenstern 2001), and our experiments support this assertion. Released and accumulated in sufficient abundance, these low-viscosity supercritical fluids could facilitate lower crustal magma transport by opening tensile fractures in hot, pressurized country rock that might otherwise deform in a ductile manner.

Deep degassing of CO_2 in sub-arc magma

Dissolved CO_2 concentrations in primary, un-degassed sub-arc basaltic melts inferred from the ratio of carbon dioxide to noble gas (e.g., $CO_2/^3He$) in lavas, hydrothermal fluids, and/or volcanic gas emissions span the range from 0.4–1.3 wt% (Wallace 2004; Fischer and Marty 2004). Our solubility experiments demonstrate that dissolved CO_2 concentrations as high as 1.3 wt% are certainly feasible in mafic arc magmas residing at depths near the continental Moho.

For Pavlof volcano, petrologic models indicate that basaltic andesite melts form in a lower- to mid-crustal intrusive complex from high-alumina basaltic parents fractionating clinopyroxene, spinel, and plagioclase at depths equivalent to 500 to 1000 MPa (Mangan et al. 2009). Seismic tomography supports this petrologic interpretation: inversion of P-wave velocities from regional earthquakes reveals a crustal thickness of about 40 km and the top of a low-velocity zone, inferred to be a region of 10–15% melt, at ~20 km (McNutt and Jacob 1986). Infrequent long-period earthquakes are detected at focal depths of between 20–40 km, presumed to be triggered by quasi-steady fluxing of basaltic magmas, and by release and escape of their exsolved CO_2-rich fluids, in a deep intrusive complex (Power et al. 2004). Using published magma-supply estimates for Pavlof of 10^6–10^7 m^3/year characterizing the last several decades (McNutt and Beavan 1987; Waythomas et al. 2017), liberation of 10^7–10^8 kg of magmatic CO_2 per year is possible within a crustal volume of ~3.5×10^8 m^3, assuming originally CO_2-saturated basalt or basaltic-andesite melt at 40 km, 2680 kg/m^3 melt density, and that the magmas degas large fractions of their CO_2 either by ascent and decompression or by large extents of solidification.

Basaltic melt inclusions (MIs) are rare in Pavlof's eruption scoria and the few analyzed samples offer little additional insight into the original concentration of CO_2 in its source magma. Mafic MIs contain ≤2.5 wt% and ≤550 ppm dissolved H_2O and CO_2, respectively (Anderson 1982; M. Zimmer, personal com-

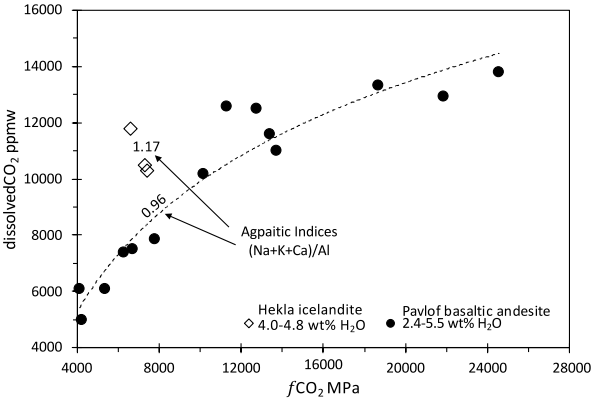

Figure 10. Comparison of CO_2 concentrations in hydrous basaltic andesite (this study) and icelandite (Jakobsson 1997) covering experimental f_{CO_2} between 4000–25 000 MPa (720–1200 MPa total pressure); CO_2-rich fluid for both suites are in the range $X_{CO_2}^{fluid}$ = 0.66–0.93. Ranges of dissolved H_2O in the experimental melts are as shown. For consistency, the published Jakobsson f_{CO_2} values were recast using the model of Churakov and Gottschalk (2003a, 2003b). Dashed line is a curve fit to the subset of the Pavlof data plotted.

munication, 2006; Zimmer et al. 2010), but were trapped at low pressures in olivine and magnetite crystallizing at <200 MPa in sub-volcanic feeders (Mangan et al. 2009).

The Pavlof experimental results allow for CO_2 concentrations in its basaltic andesite liquids in the range of ~1.4–0.1 wt% for magmas residing at ~45 to 15 km depth, respectively. A broad survey of melt-inclusion CO_2 concentrations published for hydrous, subduction-related basaltic compositions are mostly in the range 500–1500 ppm (see Fig. 9 in Métrich and Wallace 2008), which when considered in tandem with the experiments herein, suggest that substantial CO_2-rich degassing occurs prior to MI entrapment in most arc magmas.

Acknowledgments

The design and interpretation of our experiments benefited from numerous discussions with Jake Lowenstern, Dawnika Blatter, Bill Evans, and Jennifer Lewicki. We appreciate Mindy Zimmer for sharing her unpublished melt inclusion data. We thank Gary Landis for his effort to extract compositions on gas/fluids using with micro-ICPMS. Peer reviews by Jake Lowenstern, Kurt Roggensack, and Antonio Paonita, and Antonio Acosta-Vigil's editorial comments and handling are greatly appreciated.

Funding

This study was funded by the U.S. Geological Survey, Volcano Hazards Program with additional support from the Woods Hole Oceanographic Institution, Department of Geology and Geophysics, and the University of Lausanne, Institute of Mineralogy and Geochemistry. Any use of trade, firm, or product names is for descriptive purposes only and does not imply endorsement by the U.S. Government.

References cited

Allison, C.M., Roggensack, K., and Clarke, A.B. (2019) H_2O-CO_2 solubility in alkali-rich mafic magmas; new experiments at mid-crustal pressures. Contributions to Mineralogy and Petrology, 174, 58. https://doi.org/10.1007/s00410-019-1592–4.

Anderson, A.T. (1982) Parental basalts in subduction zones: implications for continental evolution. Journal of Geophysical Research, 87, 7047–7060.

Armstrong, J.T. (1995) CITZAF: A package of correction programs for the quantitative electron microbeam X-ray analysis of thick polished materials, thin films, and particles. Microbeam Analysis, 4, 177–200.

Behrens, H., Misiti, V., Freda, C., Vetere, F., Botcharnikov, R.E., and Scarloto, O. (2009) Solubility of H_2O and CO_2 in ultrapotassic melts at 1200 and 1250 °C and pressure from 50–500 MPa. American Mineralogist, 94, 105–120. doi:10.2138/am.2009.2796.

Bista, S., Stebbins, J.F., Hankins, W.B., and Sisson, T.W. (2015) Aluminosilicate melts and glasses at 1 to 3 GPa: Temperature and pressure effects on recovered structural and density changes. American Mineralogist, 100, 2298–2307, doi.org/10.2138/am-2015–5258.

Blatter, D.L., Sisson, T.W., and Hankins, W.B. (2013) Crystallization of oxidized, moderately hydrous arc basalt at mid-to-lower-crustal pressures: Implications for andesite genesis. Contributions to Mineralogy and Petrology, 166, 861–886.

Bohlen, S.R. (1984) Equilibria for precise calibration and a frictionless furnace assembly for the piston-cylinder apparatus. Neues Jahrbuch für Mineralogie. Monatshefte, 4, 404–412.

Botcharnikov, R., Freise, M., Holtz, F., and Behrens, H. (2005) Solubility of C-O-H mixtures in natural melts: new experimental data and application to a range of models. Annals of Geophysics, 48, 633–645.

Bottinga, Y., and Javoy, M. (1991) The degassing of Hawaiian tholeiite. Bulletin of Volcanology, 53, 73–85.

Brooker, R., Holloway, J.R., and Hervig, R. (1998) Reduction in piston-cylinder experiments: The detection of carbon infiltration into platinum capsules. American Mineralogist, 83, 985–994.

Burnham, C.W. (1979) The importance of volatile constituents. In H.S. Yoder, Ed., The evolution of igneous rocks, Fiftieth Anniversary Perspectives, p. 1077–1084, Princeton University Press.

Churakov, S.V., and Gottschalk, M. (2003a) Perturbation theory based equation of state for polar molecular fluids: I. Pure fluids. Geochimica et Cosmochimica Acta, 67, 2397–2414.

——— (2003b) Perturbation theory based equation of state for polar molecular fluids: II. Fluid mixtures. Geochimica et Cosmochimica Acta, 67, 2415–2425.

Costantini, L., Bonadonna, C., Houghton, B.F., and Wehrmann, H. (2009) New physical characterization of the Fontana Lapilli basaltic Plinian eruption Nicaragua. Bulletin of Volcanology, 71, 337. doi:10.1007/s00445-008-0227–9.

Costantini, L., Houghton, B.F., and Bonadonna, C. (2010) Constraints on eruption dynamics of basaltic explosive activity derived from chemical and microtextural study: the example of the Fontana Lapilli Plinian eruption, Nicaragua. Journal of Volcanology and Geothermal Research, 189, 207–224. doi:10.1016/jvolgeores.2009.11.008.

Dixon, J.E., Stolper, E.M., and Holloway, J.R. (1995) An experimental study of water and carbon dioxide solubilities in Mid-Ocean Ridge basaltic liquids. Part I: Calibration and solubility models. Journal of Petrology, 36, 1607–1631.

Duan, X. (2014) A general model for predicating the solubility behavior of H_2O-CO_2 fluids in silicate melts over a wide range of pressure, temperature, and compositions. Geochimica et Cosmochimica Acta, 125, 582–609.

Epel'baum, M.B., Bababashov, I.V., and Salova, T.P. (1973) Surface tension of felsic magmatic melts at high temperature and pressures, Geokhimiya, 3, 461–464.

Fine, G., and Stolper, E. (1986) Dissolved carbon dioxide in basaltic glasses: Concentrations and speciation. Earth and Planetary Sciences Letters, 76, 263–278.

Fischer, T.B., and Marty, B. (2004) Volatile abundances in sub-arc mantle: Insights from volcanic and hydrothermal gas discharges. Journal of Volcanology and Geothermal Research, 140, 205–216.

Ghiorso, M.S., and Gualda, G.A.R. (2015) An H_2O-CO_2 mixed fluid saturation model compatible with rhyolite-MELTS. Contributions to Mineralogy and Petrology, 169, 53. https://doi.org/10.1007/s00410-015-1141-8.

Hamilton, D.L., Burnham, C.W., and Osborn, E.F. (1964) The solubility of water and effects on oxygen fugacity and water content on crystallization in mafic magmas. Journal of Petrology, 5, 21–39.

Holland, T., and Powell, R. (1991) A Compensated-Redlich-Kwong (CORK) equation for volumes and fugacities of CO_2 and H_2O in the range 1 bar to 50 kbar and 100–1600°C. Contributions to Mineralogy and Petrology, 109, 265–273.

——— (2003) Activity-composition relations for phases of petrological calculations: An asymmetric multicomponent formulation. Contributions to Mineralogy and Petrology, 145, 492–501.

Holloway, J.R., Dixon, J.E., and Pawley, A.R. (1992) An internally heated, rapid-quench, high-pressure vessel. American Mineralogist, 77, 643–646.

Iacono-Marziano, G., Morizet, Y., Le Trong, E., and Gaillard, F. (2012) New experimental data and semi-empirical parameterization of H_2O-CO_2 solubility in mafic melts. Geochimica et Cosmochimica Acta, 97, 1–23. doi:10.1016/j.gca.2012.08.035.

Iacovino, K., Moore, G., Roggensack, K., Oppenheimer, C., and Kyle, P. (2013) H_2O-CO_2 solubility in mafic alkaline magma: applications to volatile sources and degassing behavior at Erebus volcano, Antarctica. Contributions to Mineralogy and Petrology, 166, 845–860. doi:10.1007/s00410-013-0877-2.

Jakobsson, S. (1997) Solubility of water and carbon dioxide in an icelandite at 1400 °C and 10 kilobars. Contributions to Mineralogy and Petrology, 127, 129–135.

Jarosewich, E., Nelen, J.A., and Norberg, J.A. (1980) Reference standards for electron microprobe analysis. Geostandards Newsletter, 4, 43–47.

King, P.L., and Holloway, J.R. (2002) CO_2 solubility and speciation in intermediate (andesitic) melts: the role of H_2O and composition. Geochimica et Cosmochimica Acta, 66, 1627–1640.

Kress, V.C., and Carmichael, I.S.E. (1988) Stoichiometry of the iron oxidation reaction in silicate melts. American Mineralogist, 73, 1267–1274.

Lautze, N.C., Sisson, T.W., Mangan, M.T., and Grove, T.L. (2010) Segregating gas from melt: an experimental study of the Ostwald ripening of vapor bubbles in magmas. Contributions to Mineralogy and Petrology, 161, 331–347.

Lesne, P., Scaillet, B., Pichavant, M., and Beny, J.-M. (2011) The carbon dioxide solubility in alkali basalts: an experimental study. Contributions to Mineralogy and Petrology, 162, 153–168.

Liu, X., O'Neill, H.St.C., and Berry, A.J. (2006) The effects of small amounts of H_2O, CO_2 and Na_2O on the partial melting of spinel lherzolite in the system CaO-MgO-Al_2O_3-$SiO_2 \pm H_2O \pm CO_2 \pm Na_2O$ at 1.1 GPa. Journal of Petrology, 47, 409–434. doi:10.1093/petrology/egi081.

Lowenstern, J.B. (2001) Carbon dioxide in magmas and implications for hydrothermal systems. Mineralium Deposita, 36, 490–502. doi:10.1007/s001260100185.

Mangan, M.T., Miller, T., Waythomas, C., Trusdell, F., Calvert, A., and Layer, P. (2009) Diverse lavas from closely spaced volcanoes drawing from a common parent: Emmons Lake Volcanic Center, Eastern Aleutian Arc. Earth and Planetary Science Letters, 287, 363–372. doi:10.1016/j.epsl.2009.08.018.

Mangan, M.T., Cashman, K.V., and Swanson, D.A. (2014) The dynamics of Hawaiian-style eruptions: A century of study. In M.P. Poland, T.J. Takahashi, and C.M. Landowski, Eds., Characteristics of Hawaiian Volcanoes. U.S. Geological Survey Professional Paper 1801, 323–354. http://dx.doi.org/10.3133/pp1801.

Mastin, L.G. (1997) Evidence for water influx from a caldera lake during the explosive hydromagmatic eruption of 1790, Kilauea Volcano, Hawaii. Journal of Geophysical Research, 102-B9, 20093–20109.

Mastin, L.G., Christiansen, R.L., Thornber, C., Lowenstern, J.B., and Beeson, M. (2004) What makes hydromagmatic eruptions violent? Some insights from the Keanakakoi Ash, Kilauea Volcano, Hawaii. Journal of Volcanology and Geothermal Research, 137, 15–31.

McNutt, S.R., and Beavan, R.J. (1987) Eruptions of Pavlof Volcano and their possible modulation by ocean load and tectonic stresses. Journal of Geophysical Research, 92-B, 11,509–11,523.

McNutt, S.R., and Jacob, K.H. (1986) Determination of large-scale velocity struc-

ture of the crust and upper mantle in the vicinity of Pavlof volcano, Alaska. Journal of Geophysical Research, 91-B5, 5013–5022.

Métrich, N., and Wallace, P.J. (2008) Volatile abundances in basaltic magma and their degassing paths tracked by melt inclusions. In K.D. Putirka and F.J. Tepley III, Eds., Minerals, Inclusions and Volcanic Processes, 69, 363–402. Reviews in Mineralogy and Geochemistry, Mineralogical Society of America, Chantilly, Virginia.

Moore, G. (2008) Interpreting H_2O and CO_2 contents in melt inclusions: Constraints from solubility experiments and modeling. In K.D. Putirka and F.J. Tepley III, Eds., Minerals, Inclusions and Volcanic Processes, 69, 333–361. Reviews in Mineralogy and Geochemistry, Mineralogical Society of America, Chantilly, Virginia.

Ni, H., and Keppler, H. (2013) Carbon in silicate melts. In R.M. Hazen, A.P. Jones, and J.A. Baross, Eds., Carbon in Earth, 75, 251–287. Reviews in Mineralogy and Geochemistry, Mineralogical Society of America, Chantilly, Virginia.

Nye, C.J., and Reid, M.R. (1986) Geochemistry of primary and least fractionated lavas from Okmok Volcano, central Aleutians: Implications for arc magmagenesis. Journal of Geophysical Research, 91, 10271–10287.

Papale, P., Moretti, R., and Barbato, D. (2006) The compositional dependence of the saturation surface of H_2O + CO_2 fluids in silicate melts. Chemical Geology, 229, 78–95.

Polacci, M., Baker, D., Mancini, L., Tromba, G., and Zanini, F. (2006) Three-dimensional investigation of volcanic textures by X-ray microtomography and implication for conduit processes. Geophysical Research Letters, 33, L13312. doi:10.1029/2006GL026241.

Power, J.A., Stihler, S.D., White, R.A., and Moran, S.C. (2004) Observations of deep long-period (DLP) seismic events beneath Aleutian arc volcanoes: 1989–2002. Journal of Volcanology and Geothermal Research, 138, 243–266.

Sable, J.E., Houghton, B.F., Del Carlo, P., and Coltelli, M. (2006) Changing conditions of magma ascent and fragmentation during the Etna 122 BC basaltic Plinian eruption; evidence from clast microtextures. Journal of Volcanology and Geothermal Research, 158, 333–354. doi:10:1016/j.jvolgeores.2006.07.006.

Saxena, S.K., and Fei, Y. (1987) High pressure and high temperature fluid fugacities. Geochimica et Cosmochimica Acta, 51, 783–791.

Shishkina, T.A., Botcharnikov, R.E., Holtz, F., Almeev, R.R., and Portnyagin, M.V. (2010) Solubility of H_2O- and CO_2-bearing fluids in tholeiitic basalts at pressures up to 500 MPa. Chemical Geology, 277, 115–125. doi:10.1016/j.chemgeo.2010.07014.

Sisson, T.W., Ratajeski, K., Hankins, W.B., and Glazner, A.F. (2005) Voluminous granitic magmas from common basaltic sources. Contributions to Mineralogy and Petrology, 148, 635–661. doi:10.1007/s004100050155.

Ussing, N.V. (1912) Geology of the country around Julianehaab, Greenland. Meddelelser om Grønland, 38, 426pp.

Vennemann, T.W., and O'Neil, J.R. (1993) A simple and inexpensive method of hydrogen isotope and water analyses of minerals and rocks based on zinc reagent. Chemical Geology, 103, 227–234.

Vetere, F., Botcharnikov, R.E., Holtz, F., Behrens, H., and De Rosa, R. (2011) Solubility of H_2O and CO_2 in shoshonitic melts at 1250 °C and pressures from 50 to 400 MPa: Implications for Campi Flegrei magmatic systems. Journal of Volcanology and Geothermal Research, 202, 251–261. doi:10.1016/j.volgeores.2011.03.002.

Wallace, P.J. (2004) Volatiles in subduction zone magmas: concentrations and fluxes based on melt inclusion and volcanic gas data. Journal of Volcanology and Geothermal Research, 140, 217–240.

Waythomas, C.F., Haney, M.M., Wallace, K.L., Cameron, C.E., and Schneider, D.J. (2017) The 2014 eruptions of Pavlof Volcano, Alaska. U.S. Geological Survey Scientific Investigations Report 2017-5129, 27 p.

Zhang, Y., and Ni, H. (2010) Diffusion of H, C, and O components in silicate melts. In Y. Zang and D.J. Cherniak, Eds., Diffusion in Minerals and Melts, 72, 171–225. Reviews in Mineralogy and Geochemistry, Mineralogical Society of America, Chantilly, Virginia.

Zimmer, M.M., Plank, T., Hauri, E.H., Yogodzinski, G.M., Stelling, P., Larsen, J., Singer, B., Jicha, B., Mandeville, C., and Nye, C.J. (2010) The role of water in generating the calc-alkaline trend: New volatile data for Aleutian magmas and a new tholeiitic index. Journal of Petrology, 51, 2411–2444. doi:10.1093/petrology/egq062.

Manuscript received March 30, 2020
Manuscript accepted July 29, 2020
Manuscript handled by Antonio Acosta-Vigil